Applied Catalysis B: Environmental 268 (2020) 118549

Contents lists available at ScienceDirect

Applied Catalysis B: Environmental

journal homepage: www.elsevier.com/locate/apcatb

Novel magnetic rod-like Mn-Fe oxycarbide toward peroxymonosulfate activation for efficient oxidation of butyl paraben: Radical oxidation versus singlet oxygenation

Jia-Cheng E. Yang[a,b,c,d], Yuan Lin[b], Hui-Hui Peng[b,e], Baoling Yuan[e,**], Dionysios D. Dionysiou[f], Xiao-Dan Huang[d,e], Dan-Dan Zhang[b], Ming-Lai Fu[a,b,*]

[a] Key Laboratory of Urban Pollutant Conversion, Chinese Academy of Sciences (CAS), No. 1799, Jimei Avenue, Xiamen, 361021, China
[b] Institute of Urban Environment (IUE), Chinese Academy of Sciences (CAS), No. 1799, Jimei Avenue, Xiamen, 361021, China
[c] University of Chinese Academy of Sciences (UCAS), No. 19, Yuquan Road, Shijingshan District, Beijing, 100049, China
[d] Fujian Provincial Key Laboratory of Ecology-Toxicological Effects & Control for Emerging Contaminants, Putian University, No. 1133, Xueyuan Middle Street, Chengxiang District, Putian, 351100, China
[e] College of Civil Engineering, Huaqiao University, No. 668, Jimei Avenue, Xiamen, 361021, China
[f] Environmental Engineering and Science Program, Department of Chemical and Environmental Engineering (ChEE), University of Cincinnati, Cincinnati, OH, 45221-0012, USA

ARTICLE INFO

Keywords:
Magnetic Mn-Fe oxycarbide
Peroxymonosulfate
Butyl paraben
Emerging contaminants
Radical oxidation

ABSTRACT

A new peroxymonosulfate (PMS) oxidation system was constructed using a novel magnetic Mn-Fe oxycarbide (mMFC) as an activator. We found that the non-metal (−C=O groups) and metal (Mn/Fe oxides) species within mMFC as dual active sites activated/catalyzed PMS synergistically to generate $SO_4^{\cdot -}$, $^{\cdot}OH$, $^1O_2$ and $O_2^{\cdot -}$, then $^1O_2$ and/or $O_2^{\cdot -}$ served as a secondary driving force to form $SO_4^{\cdot -}$ and $^{\cdot}OH$ for butyl paraben (BPB) oxidation *via* a radical reaction process. The stability of mMFC and the effects of initial pH, dosages, solution temperature and environmental conditions on BPB oxidation kinetics were probed with a proposed catalytic mechanism of mMFC toward PMS activation for BPB oxidation. The revealed radical and singlet formation/evolutions and radical-controlled BPB degradation mechanisms in mMFC/PMS system would advance our knowledge of designing novel magnetic Mn-based oxycarbides with elaborate structures/properties toward PMS activation for effective oxidation of emerging contaminants in wastewater.

1. Introduction

Triggered by an ever-increasing need for developing innovative technologies to remediate contaminated sites/waters, more attention has been paid to peroxide-based in situ chemical oxidation (PO-ISCO) technologies because of their robust oxidation abilities toward organic compounds [1–5]. Activating/catalyzing persulfate with earth-abundant transition metal oxides (e-TMO) represents one of the most potential directions for PO-ISCO technologies [6–9]. Manganese oxides (MO, as typical e-TMO) had been widely explored as PO-ISCO materials because of their low cost, easy-made, versatile structures and high oxidation/catalytic efficacy [10–12]. Nevertheless, because of the intrinsic structure defects and non-magnetism, MO suffer from two drawbacks: I) releasing Mn ions with high concentrations over their catalysis toward persulfate [13], and II) involving time-/energy-consuming processes for reuse (due to the lack of magnetism), both of which would heavily hinder their practical applications. Therefore, constructing novel Mn-based materials (NMC) with more catalytic sites, higher stability and desirable magnetism has become a new hotspot research for ISCO technologies.

Structure modulations by the methods of self-assembled coordination reactions between metal ions and structure-directed organic compounds/polymers hold a big promise to construct NMC with intriguing structures and tailor-made catalytic reactivity/chemical stability [14]. For example, recent work reported metal organic frameworks (MOF)-derived NMC toward H_2O_2/persulfate catalysis for effective organic oxidation [15,16]. In the light of existing evidence, the metal oxide species were usually considered as the main catalytic sites for persulfate

* Corresponding author at: Key Laboratory of Urban Pollutant Conversion, Institute of Urban Environment (IUE), Chinese Academy of Sciences (CAS), No. 1799, Jimei Avenue, Xiamen 361021, China.
** Corresponding author.
E-mail addresses: blyuan@hqu.edu.cn (B. Yuan), mlfu@iue.ac.cn (M.-L. Fu).

https://doi.org/10.1016/j.apcatb.2019.118549
Received 6 July 2019; Received in revised form 16 December 2019; Accepted 18 December 2019
Available online 08 February 2020
0926-3373/

catalysis towards pollutant degradation either by sole radical ($SO_4^{\cdot -}$ and/or $^{\cdot}OH$) or by nonradical process [10,11,15,16]. Although the radical and nonradical processes for contaminant oxidation had been reported [17–21], the roles of metal and non-metal active sites within NMC in persulfate catalysis has not been previously documented, especially for pyrolytic ones – which may induce radical oxidation and singlet oxygenation simultaneously. Meanwhile, the reported MOF-derived NMC are magnetism-free and their catalytic stability is not fully understood.

Aiming at endowing more robust practical ability of MO in ISCO applications, we presented novel magnetic rod-like Mn-Fe oxycarbides (mMFC, as magnetic NMC) – derived from covalent bimetal-organic frameworks using nitrilotriacetic acid (NTAA) as structure-directing and complexing agent, and probed their efficacy toward peroxymonosulfate (PMS) activation/catalysis. The use of NTAA here is due to the strong coordination capacities of its tricarboxylic groups with Mn/Fe ions [22], while the combination of Fe with Mn to form covalent bimetal-organic composite is conducive to the formation of magnetism. So, compared to nonmagnetic MO, much higher stability for mMFC with desirable magnetism could be expected. Considering the fact that mMFC are carbon-rich NMC with delicate structures, we thus hypothesized that mMFC in principle would possess the integrated characteristics of carbonaceous materials and MO, which may activate/catalyze PMS to form various reactive oxygen species (ROS, probably like $SO_4^{\cdot -}$, $^{\cdot}OH$, $^1O_2$ and/or $O_2^{\cdot -}$) simultaneously and therefore induce a distinctive way for effective contaminant oxidation.

To verify our hypothesis, extensive experiments regarding the physicochemical characterization, activation/catalysis efficacy and mechanism of mMFC toward PMS, and the ROS formation/evolution were performed. As an asymmetric peroxide, PMS (i.e., commercial Oxone®, $KHSO_5$•$0.5KHSO_4$•$0.5K_2SO_4$) was used as a model PS is due to its high thermodynamic stability, easy to activate and widely used for water treatments [23–25]. Because of its frequent occurrence in the aquatic environment and potential adverse effects on human health [26], butyl paraben (BPB) was selected as a representative emerging contaminant to assess the performance of mMFC towards PMS activation/catalysis. We believe that this work will enhance our knowledge toward rationally designing magnetic NMC with sophisticated structures/properties for PO-ISCO applications and manipulating ROS formation for effective destruction of emerging organic contaminants from water.

2. Materials and methods

2.1. Chemicals

All the chemicals, unless noted otherwise, were of analytical grade or better and used without further purification.

2.2. Materials synthesis

A combined method of solvothermal and calcination process was used to fabricate mMFC [22]. Typically, 40 mM $FeSO_4{\cdot}7H_2O$, 20 mM $MnSO_4{\cdot}H_2O$ and 40 mM NTAA were first dissolved in 160 mL of a mixed water-isopropanol solution (the volume rate of water/isopropanol (v/v), 3/1) by vigorous stirring at room temperature (298 ± 2 K) for at least 24 h; Secondly, the solution was transferred into a Teflon autoclave (200 mL), followed by heating it at 453 K in an electric oven for 10 h; Then, the obtained product was cross-washed with DI water and ethanol for at least 5 times by filtration, followed by drying it at 343 K overnight; Lastly, the samples after grinding were subjected to calcination at 623 K for 2–8 h in static air. The samples obtained were donated as mMFC-t, where t represents the calcination time (h). For comparison, magnetic Mn-Fe spinel oxide was also prepared and marked as mMFS (see details in Text S1 in the Supplementary materials).

2.3. Experimental methods

Unless explicitly stated, all batch experiments were carried out in 100-mL flat conical flasks (containing 80 mL aqueous solutions). At predetermined time intervals, BPB samples (2 mL) were taken and quickly quenched with 0.5 mL ethanol, followed by filtering using 0.45 μm hydrophilic cellulose acetate membranes. The residual concentrations for BPB samples were analyzed by high performance liquid chromatography (HPLC) (Agilent 1260, USA) system at a flow rate of 1 mL/min and 303 K (with a mobile phase of acetonitrile/water (55/45, v/v) and a detecting wavelength at 254 nm). Prior to conducting experiments, HNO_3 and NaOH solutions were used to carefully adjust the initial solution pH. All experiments were carried out in duplicate or triplicate in a rotary vibrator at 300 rpm under aerobic conditions (298 ± 2 K). All data were reported in an average value with 95 % of confidence level. In addition, the reusability of mMFC-6 was tested with the help of magnet and a simple drying method. In details, the used mMFC-6 was first washed with DI water at least 3 times, then dried at 333 K overnight in static air; afterwards, the regenerated mMFC-6 was subjected to the next experiment. The ultimate concentrations of Mn/Fe ions in solutions were measured by inductively coupled plasma optical emission spectroscopy (ICP-OES) (Agilent 7500cx, USA). Other information on materials characterizations and the tests of electron paramagnetic resonance (EPR) and BPB oxidation products can be found in Text S2.

3. Results and discussion

3.1. Physicochemical features of mMFC

3.1.1. Crystal and pore structures

As depicted in Fig. 1(a), all mMFC samples possess similar X-ray diffraction (XRD) patterns, and all the patterns agree well with those of $Fe_{24}O_{32}$ (JCPDS: 00-2320). Two of diff ;raction peaks (marked by blue star) can be index to that of MnOOH (JCPDS: 74-1049) and MnO_2 (JCPDS: 14-0644). Note that Mn ions within mMFC also prefer occupying the octahedral sites to form crystallized $(Mn,Fe)_{24}O_{32}$ and/or $(Mn,Fe)_3O_4$, which have similar structure features with $Fe_{24}O_{32}$ or Fe_3O_4 [27]. The N_2 adsorption/desorption isotherms of mMFC with capillary condensations at a relative pressure range of 0.65–0.95 (Fig. S1(a)) imply the presence of their mesopore features. The Brunauer–Emmett–Teller (BET) surface areas, pore sizes and Barrett–Joyner–Halenda pore volumes of mMFC are in the range of 132.66–179.63 m^2/g, 11.98–16.60 nm and 0.54– 0.56 cm^3/g, respectively (Table S1). In comparison, the surface areas of mMFC are more than two times higher than that of mMFS. The crystal and pore structures of mMFC precursor are provided in Text S3 and Fig. S2(a, b).

3.1.2. Spectroscopic characteristics

Fig. 1(b) shows the Fourier transform infrared (FT-IR) spectra of mMFC and mMFS. The peaks at 1629–1631 cm^{-1} are due to the stretching vibrations of −C═O groups bonded/adsorbed with metal species [28]. The peaks at 456–487 cm^{-1} and 561–572 cm^{-1} are ascribed to the vibrations of Mn/Fe−O bonds at octahedral and tetrahedral sites in the spinel structure, respectively, confirming the presence of $Fe_{24}O_{32}$ or $(Mn,Fe)_{24}O_{32}$ within mMFC and mMFS [27]. The peaks at 634–638 cm^{-1} are related to Mn/Fe−O bonds within Mn-Fe oxides [27,29], while the peaks in the range of 1384 cm^{-1}, 1049–1062 cm^{-1} and 1118–1160 cm^{-1} are attributed to the combined results of the stretching vibrations of C−H and/or C−O bonds and the deformation vibrations of −OH groups [30,31]. Fig. S1(b) clearly depicts that mMFC and mMFS possess four distinctive Raman-active phonon models, i.e., $T_{2g(1)}$ (209–218 cm^{-1}), E_g (267–273 cm^{-1}), $T_{2g(2)}$ (356–382 cm^{-1}) and A_{1g} (593–616 cm^{-1}), which are indicative of the translatory motion of FeO_4, the symmetric/asymmetric bends of O with respect to Fe/Mn, the asymmetric stretch of Fe/Mn and O, and the

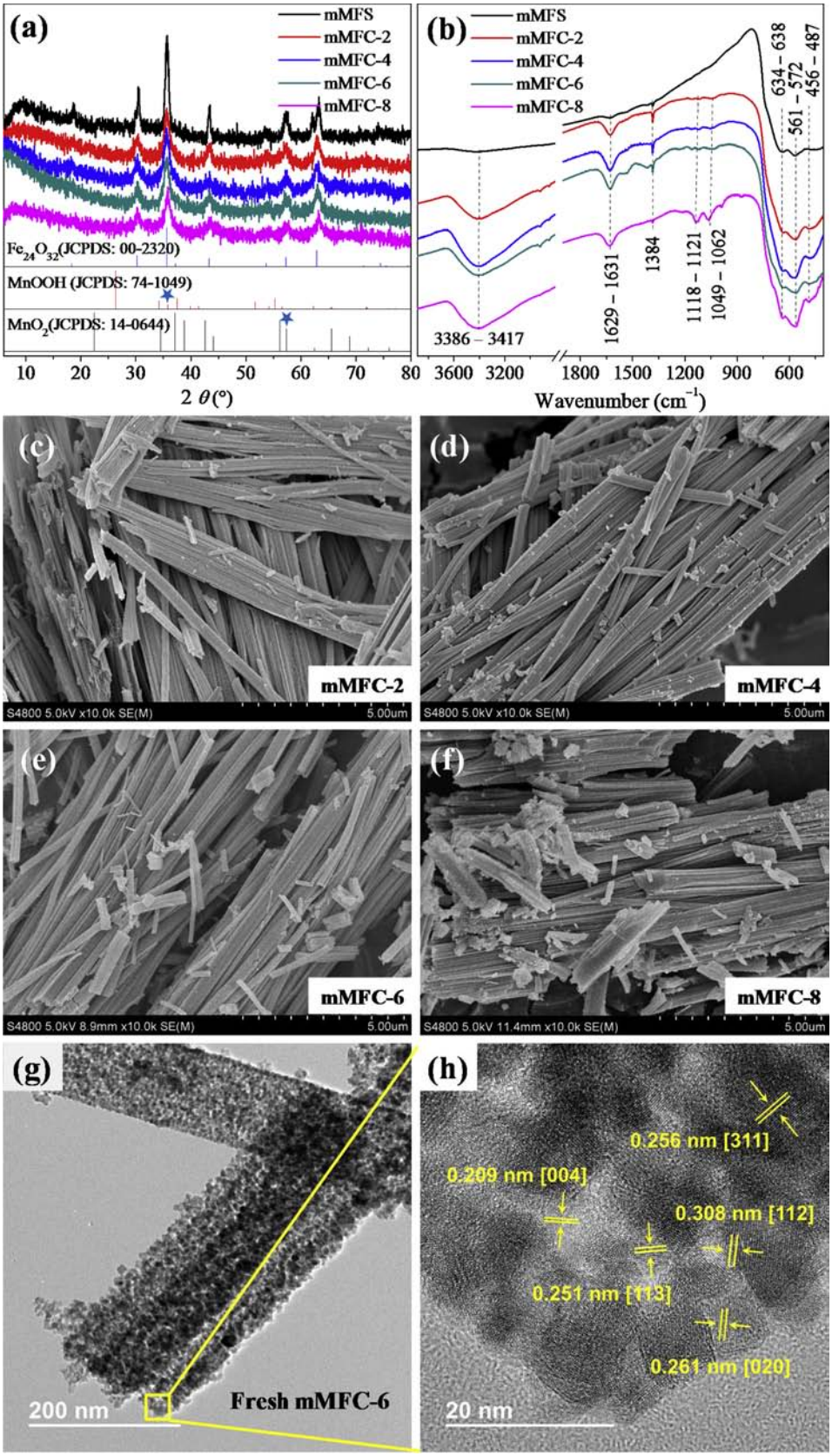

Fig. 1. XRD (a) and FT-IR (b) spectra of mMFCs and mMFS, SEM images of mMFC-2 (c), mMFC-4 (d), mMFC-6 (e) and mMFC-8 (f), and TEM images of fresh mMFC-6 (g, h).

symmetric stretch of O atoms along Fe−O bonds, respectively [32,33] (More information on spectroscopic characteristics of mMFC precursor can be found in Text S3 and Fig. S2(c, d)).

3.1.3. Morphological structures

The surface morphologies of mMFC are shown in Fig. 1(c–f). It is obvious that mMFC have intrinsic rod/strip-like structures consisted of virous Mn-Fe wires (tightly coupled with each other) with 2–20 μm in length and 0.1–1 μm in width (0.6 μm in average width). Apparently, mMFC mimicked the intrinsic rod-like topology structure of its precursor (cf. Fig. S3). Transmission electron microscopy (TEM) characterizations (Figs. 1(g, h) and S4) demonstrate that the rod-like mMFC-6 consists of both abundant porous networks and irregular nano-crystals with the size of about 8–17 nm. The transparent dots in mMFC-6 are indicative of the porous nature. Generally, the porous features of mMFC observed by scanning electron microscopy (SEM) and TEM images verify the results of BET characterizations. In the high-resolution TEM (Fig. 1(h)), the inter-planar spacings with 0.209 nm, 0.251 nm, 0.256 nm, 0.261 nm and 0.308 nm are due to the [004] plane of $Fe_{24}O_{32}$ (JCPDS: 00-2320), [113] plane of $Fe_{24}O_{32}$ (JCPDS: 00-2320), [311] plane of $MnFe_2O_4$ (JCPDS: 10-0319), [020] plane of MnOOH (JCPDS: 74-1049), and [112] plane of Mn_3O_4 (JCPDS: 24-0734), respectively. Fig. S4 shows the surface morphology information of mMFC-6 exist after PMS activation. These results indicate that Mn and Fe within mMFC-6 exist in various (hydro)oxide states, which is coincident with the survey of XRD and X-ray photoelectron spectroscopy (XPS) (cf. Figs. 1(a) and 2 (a–d)).

3.1.4. Surface element information

XPS survey (Fig. S5) suggests the presence of Mn, Fe, O and C elements within mMFC-6, which agrees well with the result of energy dispersive X-ray (EDX) characterization (Fig. S6). Both EDX and XPS investigations imply that the molar ratio of Fe/Mn is 2. The binding energy peaks at 710.48–710.63, 641.70–641.77, 284.80–284.84 and 529.79–529.83 eV for fresh and used mMFC-6 are assigned to the Fe $2p_{3/2}$, Mn $2p_{3/2}$, C 1s and O 1s, respectively [34]. In comparison to the peak at 710.48 eV for fresh mMFC-6, the shift of the corresponding peaks by 0.15 eV for used sample indicates the enhanced electronic interactions of surface Fe-O bonds [34], which probably results from the electron transfer from Fe species to PMS. Similar shifts of binding energy were also found for Mn $2p_{3/2}$ and O 1s, while reverse shift for C 1s was observed. It is worth mentioning that the degree of the shifts for Mn $2p_{3/2}$, C 1s and O 1s was very weak, which indicates the high catalytic stability of mMFC-6 toward PMS.

For Mn 2p spectra (Fig. 2(a)), the spectrum of fresh mMFC-6 can be well fitted with three sub-peaks. The peaks at 640.93 eV and 642.10 eV indicate that Mn^{3+} species exist in more than one coordination forms in fresh sample [35]. The peak of 640.93 eV is attributed to the presence of Mn_2O_3, while that of 642.10 eV is due to the formation of manganite (MnOOH), manganese oxyacetate ($MnOCH_3COO$) or/and manganese hydroxyacetate ($Mn(OH)CH_3COO$) [35,36]. The peak at 642.68 eV shows the formation of MnO_2 (birnessite). After catalyzing PMS, the spectrum of used mMFC-6 can be well fitted with three sub-peaks of 640.85, 642.01 and 643.51 eV, corresponding to Mn_2O_3, MnO_2 and MnO_2, respectively. The average valence of Mn for fresh and aged mMFC-6 samples is 3.39 and 3.80, respectively.

For Fe 2p spectra (Fig. 2(b)), the spectra show the main peaks at 710.48–710.63 eV with the associated shake-up satellites at about 718.35 eV, suggesting the presence of Fe^{3+}. The Fe $2p_{3/2}$ spectrum of fresh mMFC-6 can be fitted by three sub-peaks of 709.72, 710.90 and 712.11 eV; while after reacting with PMS, the spectrum can be fitted by three sub-peaks of 709.74, 710.70 and 712.00 eV. Both of peaks at 709.72/709.74 and 710.90/710.70 eV suggest the presence of Fe_2O_3 (either α-Fe_2O_3 or γ-Fe_2O_3) [36]. The peak of 712.11 is due to the formation of $FeCO_3$ within mMFC-6, while that at 712.00 is attributed to Fe^{3+} [36]. The average valence of Fe for fresh and aged mMFC-6 samples is 2.69 and 3.00, respectively.

For C 1s spectra (Fig. 2(c)), the spectra can be fitted by three sub-peaks centered at 284.61–284.70, 285.57–286.37 and 288.55–288.70 eV, which clearly suggest the existence of −C−C/H, −C − OH/−C═O and −O−C═O bonds within mMFC-6 [28,37], while for O 1s spectra (Fig. 2(d)), the fitted two peaks at 529.72–529.77 eV and 530.79–530.87 eV, assigning to lattice oxygen and surface hydroxyl, are observed. It is worth mentioning that N was not detected within EDX and XPS characterizations despite the fact that NTAA is a N-containing agent, which is probably ascribed to the formation of unstable nitric oxides and their volatilization during pyrolysis in air.

3.2. Catalytic performance of mMFC

3.2.1. Comparison with different processes

Figs. 2(e) and S7(a) clearly suggest that BPB removal by the volatilization/natural degradation, adsorption of catalysts, and sole PMS oxidation can be ruled out because of the limited removal efficiencies during the whole reaction. But, when 125 mg/l of mMFC precursors were introduced into BPB solution, about 45 % of BPB was removed. This might be due to the synergetic adsorption and co-precipitation induced by the precursors [38]. As expected, the concentrations of BPB experienced a drastic decrease when mMFC and PMS were introduced into the target solutions simultaneously (Fig. 2(e)). Meanwhile, mMFC showed calcination time-dependent catalytic performance towards PMS activation. Shortening or extending the time of calcination of mMFC precursors was not favorable for BPB removal. In the light of BET and SEM measurements, the specific surface areas and surface morphologies of mMFC did not contribute to such performance. From XRD, FT-IR and Raman characterizations (Figs. 1, S1, and Table S1), we infer that the varied crystal structures and Mn/Fe species probably regulated the catalytic performance of mMFC [39], though more evidence should be explored in future work. In comparison, only 60 % of BPB was oxidized by mMFS catalyzed PMS under the similar conditions. The superior catalysis of mMFC over mMFS is probably due to the smaller crystal size and higher surface area (Figs. 1(h), S7 and Table S1). More discussion on BPB removal by PMS activated with mMFC precursors or Fe/Mn ions and effects of dosages and solution temperature are also provided in Fig. S8(b–d) and Text S4. Considering the higher catalytic performance, mMFC-6 was chosen as a model catalyst for the following experiments.

3.2.2. Effect of pH and dissolve oxygen

Fig. 2(f) shows that, in general, mMFC-6 could maintain high catalytic efficacy towards PMS for BPB oxidation in the range of initial pH = 3.0–10.5. Considering the pH_{PZC} of mMFC-6 (~7.00), the pK_a of HSO_5^- (9.4) [40], the pK_a of BPB (8.47) [41], and the solution pH before and after reaction (Table 1), one can conjecture that the diverse electrostatic interactions between mMFC-6 and PMS/BPB could regulate the ROS generation/concentration under different initial pH, thus controlling BPB oxidation (proofed by the results of quenching experiments with ethanol (EtOH) and *tert*-butyl alcohol (TBA) under different initial pH (cf. Table S2)). Fig. S9 shows that the removal efficiency of BPB was 92 % within 75 min without N_2 purging, while only 56 % of BPB was oxidized after N_2 purging. The first-order kinetic oxidation of BPB decreased by 53.4 % after N_2 purging under the same reaction conditions for the case without purging. Based on previous work, such a phenomenon is probably due to the fact that higher O_2 concentration helps to generate more $O_2^{\cdot -}$ to activate PMS to form more $SO_4^{\cdot -}$ and/or $^{\cdot}OH$ [42,43]. The details on ROS formation and their types will be discussed later.

3.2.3. Catalytic stability

The ultimate concentrations of Fe and Mn ions released from mMFC and their precursor were measured for assessing their stability. As shown in Table S3, the concentrations of Mn and Fe ions released from mMFC were below 0.05 and 0.24 mg/L, respectively, far below the

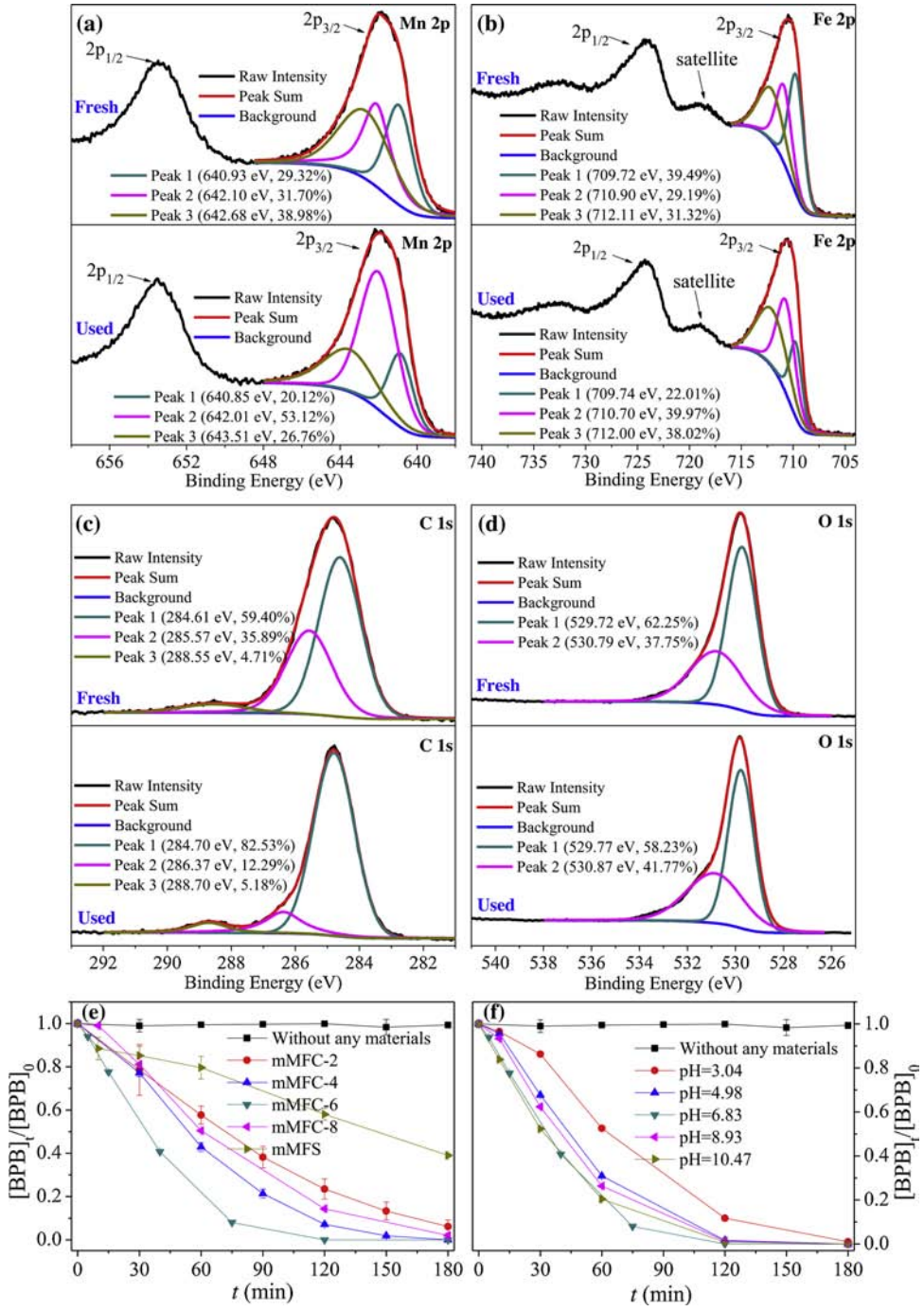

Fig. 2. High-resolution XPS spectra and fitting peaks of (a) Mn 2p, (b) Fe 2p, (c) C 1s and (d) O 1s of fresh and used mMFC-6. (e) BPB oxidation degradation by activated PMS with mMFCs and mMFS and (f) effects of initial pH on BPB oxidation degradation by mMFC-6/PMS system ($[Materials]_0$ = 125 mg/L, $[BPB]_0$ = 25.74 μM, $[PMS]_0$ = 2 mM, $[pH]_0$ = 6.83 ± 0.20 (unless otherwise noted), T = 298 ± 2 K). The error bars in symbols, unless otherwise mentioned, represent the ranges of multiple measurements ($P < 0.05$).

Table 1
BPB oxidation by the mMFC-6/PMS system under real environmental conditions.

Samples	Parameters for water quality							Removal efficiency (%) §
	Initial pH	TOC (mg/L)	$NH_4^+ - N$ (mg/L)	TN (mg/L)	TP (mg/L)	Turbidity	DO (mg/L)	
Real Water A	7.19	4.32	0.03	0.47	0.00	2.20	7.02	73 %
Real Water B	9.13	72.15	0.09	2.51	0.04	32.20	6.78	81 %

Notes: § means the removal efficiency of BPB at the reaction time of 45 min by mMFC-6/PMS, and other conditions are similar to those of Fig. 2(e, f).

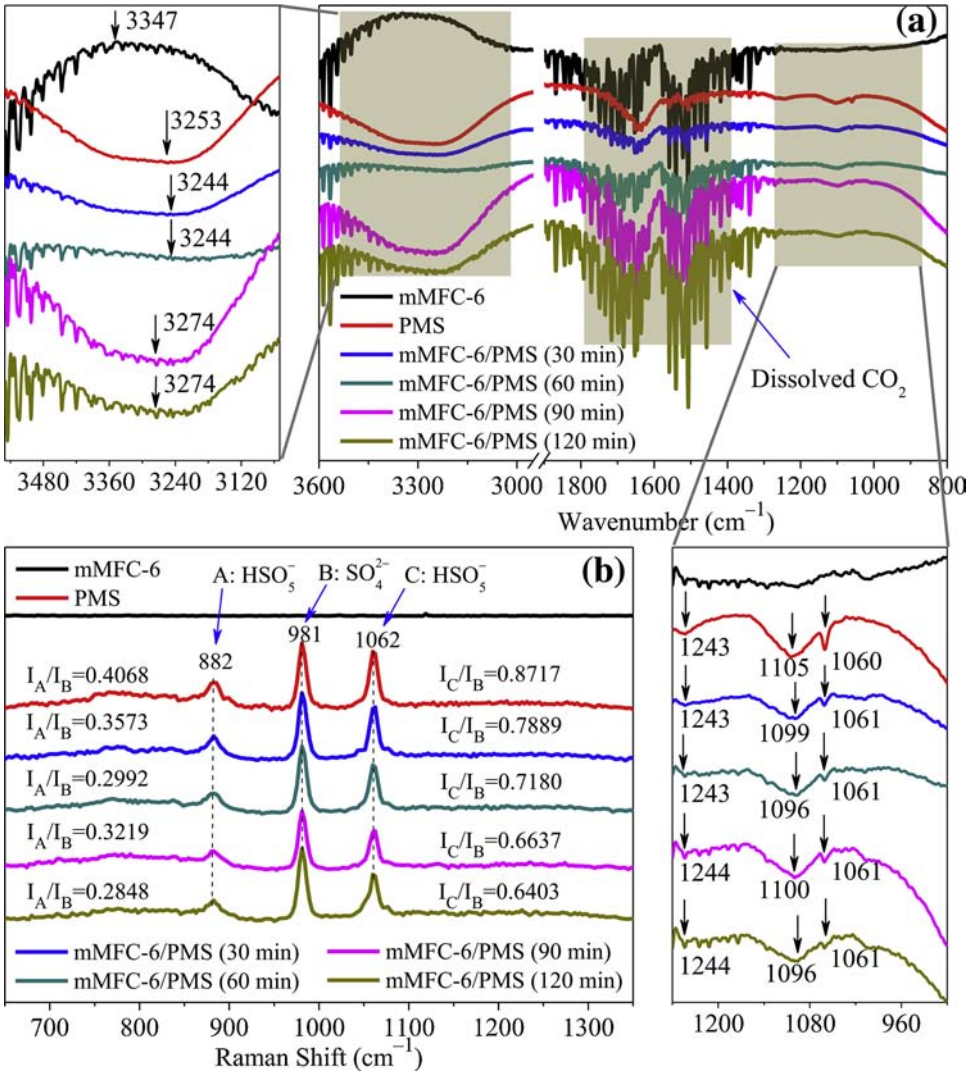

Fig. 3. In situ ATR-IR (a) and Raman (b) spectra for PMS, mMFC-6 and mMFC-6/PMS in BPB solutions ($[mMFC\text{-}6]_0$ = 2 g/L, $[BPB]_0$ = 25.74 μM, $[PMS]_0$ = 25 mM, $[pH]_0$ = 6.83 ± 0.2, T = 298 K). The spectrum of BPB solution has been subtracted prior to ATR-IR tests.

drinking water standard of China [44]. However, those for mMFC precursor were 2.46 and 6.49 mg/L, respectively. These findings imply that mMFC possess excellent stability toward PMS catalysis under different conditions, and that the calcination process is of great importance to control the metal release, thus reducing the risks of mMFC to the ecosystems. Importantly, after the third recycling by a simple method of wash and drying at low temperature (70 °C), the efficiency for BPB oxidation can still be up to 98 %, suggesting the excellent reusability of mMFC-6.

3.3. Mechanism of mMFC-6/PMS system for BPB oxidation

3.3.1. Interactions of PMS and mMFC-6

As depicted in Fig. 3(a), the peaks at 3244–3347 cm^{-1} of the in situ attenuated total reflection infrared (ATR-IR) spectra are assigned to the stretching vibrations of surface hydrogen-bonded water molecules, while those at around 1061, 1096–1105 and 1243 cm^{-1} are ascribed to the symmetric and/or asymmetric stretching vibrations of S—O bonds of PMS [45,46]. When PMS and mMFC-6 mixed together, significant shifts for the peaks of H-bonded water molecules occurred. For mMFC-6 and PMS with a reaction time of 30 min, these peaks for mMFC-6 and PMS red-shifted by 103 and 9 cm^{-1}, respectively, which was due to the formation of abundant hydrogen bonds within the adsorbed surface H_2O molecules on mMFC-6 and PMS. No shifts were detected for mMFC-6/PMS system when the reaction time was prolonged to 60 min, indicating the hydrogen bonds-based reactions had an equilibrium period; however, the equilibrium reactions were broken (i.e., blue-shifted by 30 cm^{-1} at the reaction time of 90 min) then raised to a new balance when the time increased from 90 to 120 min. According to previous work [45,47,48], we presume that such H-bonds-based reactions at the surface interface of mMFC-6 and PMS are key to the inner-sphere complexation/reaction between mMFC-6 and PMS (i.e., the PMS catalysis/activation process) and the ROS formation.

Compared to sole PMS case, a slight red shift (by 6 cm^{-1}) of the S—O bond from about 1105 to 1099 cm^{-1} was detected when PMS was activated by mMFC-6 for reacting 30 min; meanwhile, a relatively decreased intensity of the S—O bond at around 1061 cm^{-1} was also detected. The red shift is due to the decreased electron density of S—O bond – which probably resulted from the attraction of surface active sites of mMFC-6 toward the terminal H–O bond of HSO_5^-, thus increasing the elongation of its neighboring S—O bond [47]; while the decreased intensity of peak at 1061 cm^{-1} indicates the HSO_5^- decomposition over PMS activation/catalysis [45,46]. With the reaction time from 30 to 120 min, the asymmetric S—O bond at 1096–1100 cm^{-1} first slightly red-shifted after 60 min (by 3 cm^{-1}) and then blue-shifted (by 4 cm^{-1} after 90 min), followed by a red shift of 4 cm^{-1} at reaction time of 120 min. Such shift profiles imply the complex electron-donating/withdrawing reactions of mMFC-6 surface sites and HSO_5^- for

generating ROS [47].

As shown in Fig. 3(b), the peaks of in situ confocal Raman spectra at around 882 cm^{-1} (marked as A) and 1062 cm^{-1} (marked as C) are attributed to the stretching S—O bond of HSO_5^-, while the peaks at 981 cm^{-1} (marked as B) are ascribed to the stretching S—O bond of SO_4^{2-} (including HSO_4^-) [45]. It is well known that, it is $KHSO_5$ within PMS ($KHSO_5$•0.5$KHSO_4$•0.5K_2SO_4) not $KHSO_4$ or K_2SO_4, that is the precursor of free radicals [45,49]. Therefore, the intensity ratios of A/B and C/B (i.e., I_A/I_B and I_C/I_B) can be used to probe the activation process of PMS. Obviously, decreased I_A/I_B and I_C/I_B values were found when PMS and mMFC-6 mixed together. The variation profiles for I_A/I_B values followed the trend of the stretching vibrations of S—O bond around 1096–1105 cm^{-1}, suggesting the complex electron attractions of the terminal H–O bond of HSO_5^- toward its neighboring S—O bond; while, the substantially reduced I_C/I_B values from 30 to 120 min indicated the continuously decreased S—O bond off the terminal H–O bond over HSO_5^- decomposition, both of which were very important for ROS formation. It should be noted that the changes of S—O bond and hydrogen-bonded water molecules detected in operando ATR-IR and Raman spectra are highly dependent on the types of catalysts and/or activators because of the complex reactions over persulfate activation/catalysis.

XPS fitting results (cf. Fig. 2(a–d) and Section 3.1.4) imply that, after activation, the average valence of Mn and Fe within mMFC-6 increased. This is resulted from the electron-donating process from surface Mn/Fe species (as catalytic sites) to the terminal —OH groups of HSO_5^- [47], which supported the observation of the aforementioned blue shift for S—O bond. Interestingly, after catalysis, the rate of —C—OH/—C═O within mMFC-6 was found to decreased greatly (from 35.89 % to 12.29 %), while that of —C—C/H increased markedly (from 59.40%–82.53 %). Based on previous work, we concluded that ketone groups (—C═O) within mMFC-6 could also serve as active sites toward PMS catalysis [37,50], which resulted in the decreased ratio of —C═O/—C—OH [28,37]; meanwhile, the newly formed $SO_4^{\cdot-}$ and $^{\cdot}OH$ could also decrease the content of —C═O/—C—OH within mMFC-6 through the radical oxidation degradation process [51]. Additionally, an increased peak area ratio of surface hydroxyl oxygen (O_{suf}, 530.79–530.87 eV) and lattice oxygen (O_{lat}, 529.72–529.77 eV) – probably resulted from the formation of abundant OH-based Mn, Fe and/or C species – was detected. The increased ratio of O_{suf}/O_{lat} indicates the decreased defects (like oxygen vacancies) within mMFC-6 surface over PMS catalysis, which could act as a promoter to generate $O_2^{\cdot-}$ [42].

3.3.2. ROS in mMFC-6/PMS system

Quenching experiments show that, when 500 mM ethanol (EtOH) or *tert*-butyl alcohol (TBA) was added into mMFC-6/PMS system, EtOH demonstrated stronger inhibition to BPB removal than TBA (Figs. 4, S10 and Table S4), suggesting that $SO_4^{\cdot-}$ was the main ROS in mMFC-6/PMS oxidation system. Nevertheless, the lower inhibition of TBA than EtOH does not completely exclude the role of $^{\cdot}OH$ (because TBA can also react with $SO_4^{\cdot-}$ ((4.0–8.1) × 10^5 $M^{-1}s^{-1}$) (see Table S5) [52]. Further increasing EtOH and TBA concentration to 2000 mM caused a significant reduction in BPB removal Fig. 4). The removal efficiencies decreased to 17.22 % and 39.12 %, respectively for EtOH and TBA, while k_{obs} values decreased by 96.68 % and 91.37 %, respectively (Table S4), verifying $^{\cdot}OH$ as well as $SO_4^{\cdot-}$ contributed to BPB oxidation.

Despite of their high second order reaction rate constants with $^{\cdot}OH$ and $SO_4^{\cdot-}$ (Table S5), L-histidine (HD) and p-benzoquinone (BQ) had been widely used as the scavengers of $^1O_2$ and $O_2^{\cdot-}$, respectively, to probe ROS formation in persulfate-related oxidation systems [9,11,12,53]. Fig. 4 depicts that both HD and BQ inhibited BPB removal, implying that $^1O_2$ and/or $O_2^{\cdot-}$ were involved in mMFC-6/PMS system. This is because that, if $SO_4^{\cdot-}$ and $^{\cdot}OH$ were only ROS, 500 mM EtOH ($9.5 \times 10^8\ s^{-1}$, (0.8–3.9) × 10^7 s^{-1}, $1.9 \times 10^3\ s^{-1}$ and < 5 × $10^2\ s^{-1}$ for scavenging $^{\cdot}OH$, $SO_4^{\cdot-}$, $^1O_2$ and $O_2^{\cdot-}$, respectively, cf. Table S5) would show much stronger inhibition to BPB removal than 4 mM BQ ($4.8 \times 10^6\ s^{-1}$, $4 \times 10^5\ s^{-1}$, $1.52 \times 10^4\ s^{-1}$ and (3.6 − 4) × 10^6 s^{-1}, for scavenging $^{\cdot}OH$, $SO_4^{\cdot-}$, $^1O_2$ and $O_2^{\cdot-}$, respectively, cf. Table S5); however, the result is reverse (Figs. 4, S10 and Table S4). It should be noted that, with respect to quenching $^{\cdot}OH$, $SO_4^{\cdot-}$, $^1O_2$ and $O_2^{\cdot-}$, BQ would suppress BPB removal more strongly than HD (Table S5). On the contrary, HD showed stronger inhibition to BPB removal than BQ (Figs. 4, S10 and Table S4). Previous investigations noted that, besides its higher scavenging ability toward ROS, HD can also quickly react with PMS [20,21]. Therefore, it is reasonable that HD can induce higher inhibition effect than the other three quenchers (Figs. 4, S10 and Table S4).

Electron paramagnetic resonance (EPR) tests (using 5,5-dimethyl-1-pyrroline N-oxide (DMPO) and 2,2,6,6-tetramethyl-4-piperidone (TEMP) as the spin trapping reagents) were carried out to further confirm the above results. As shown in Fig. 5, when DMPO was added into mMFC-6/PMS system, a distinct four-line signal with peak strength of 1:2:2:1 for DMPO$^{\cdot}$—OH adduct and a six-line signal for DMPO$^{\cdot}$-SO_4^- adduct were detected in the ternary systems of DMPO, which provided a direct evidence for the formation of both $SO_4^{\cdot-}$ and $^{\cdot}OH$ (by the analysis of hyperfine splitting) [54–56]. The absent EPR signals in Fig. 5(a_1,a_3) imply the absence of $SO_4^{\cdot-}$ and $^{\cdot}OH$ for the case of sole BPB or mMFC-6. However, weak signals were detected for sole PMS when DMPO was introduced into BPB-containing solution, which was due to the reaction of DMPO with PMS [57]. The lower signals for sole PMS in compared with those for mMFC-6/PMS system verify the favorable role of mMFC-6 in PMS activation to form $SO_4^{\cdot-}$ and $^{\cdot}OH$. The three-line EPR spectra with equal peak intensities (Fig. 5(b)) were clearly observed using TEMP as a tripping reagent for mMFC-6/PMS binary system, suggesting the formation of $^1O_2$ [43,55,58]. Previous work indicated that direct electron abstraction from TEMP followed by

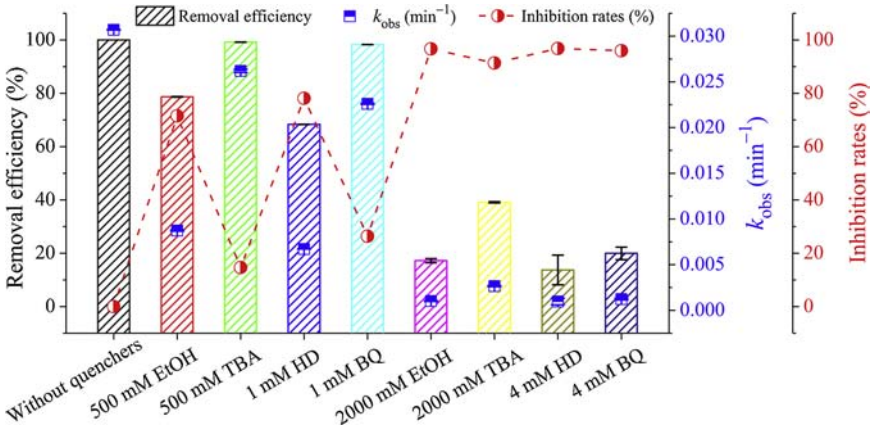

Fig. 4. Effects of different quenchers on BPB oxidation by mMFC-6/PMS system: Reaction conditions: $[mMFC\text{-}6]_0$ = 125 mg/L, $[BPB]_0$ = 25.74 μM, $[PMS]_0$ = 2 mM, $[pH]_0$ = 6.83 ± 0.20, T = 298 ± 2 K. Inhibition rate means the degree of the reduction of k_{obs} values in the presence of quenchers, compared to those without quenchers.

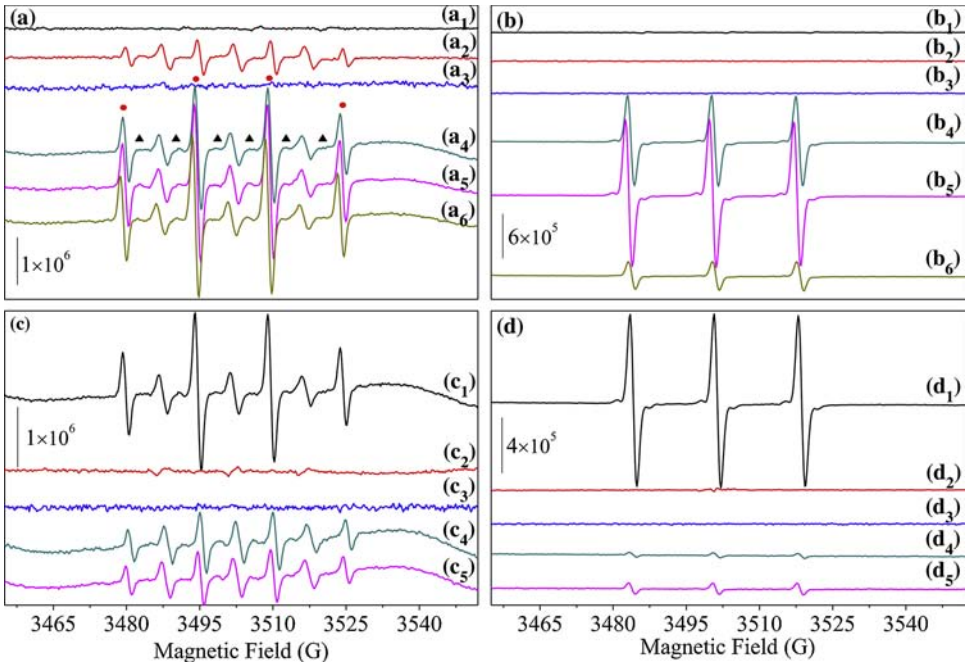

Fig. 5. EPR signals detected in BPB-containing mMFC-6/PMS related systems ((a) and (c) for DMPO$^{\cdot}$−OH (red circle) and DMPO$^{\cdot}$-$SO_4^{\cdot-}$ (black triangle) adducts, while (b) and (d) for TEMP-$^1O_2$ adducts): (a_1,b_1) for sole BPB, (a_2,b_2) for sole PMS, (a_3,b_3) for sole mMFC-6, and (a_4–a_6,b_4–b_6) for mMFC-6/PMS system at reaction time of 40, 70 and 170 min, respectively; (c_1,d_1) for mMFC-6/PMS system without quenchers, while (c_2–c_5, d_2–d_5) for 5 mM BQ, 20 mM BQ, 20 mM DMSO and 20 mM FFA, respectively ($[PMS]_0$ = 2 mM, $[BPB]_0$ = 25.74 μM, $[mMFC\text{-}6]_0$ = 125 mg/L, $[DMPO]_0$ = $[TEMP]_0$ = 0.2 M, $[pH]_0$ = 6.83 ± 0.2, T = 298 K, t = 70 min (except if noted otherwise)) (For interpretation of the references to colour in this figure legend, the reader is referred to the web version of this article).

the combination with oxygen could result in the formation of TEMPO [21], which undoubtedly produces serious interference for $^1O_2$ identification. Therefore, we conduct additional experiments to prove it. As shown in Fig. 4(b1), the signals of TEMP-$^1O_2$ adducts in sole BPB solution are very weak, 3–4 orders of magnitude lower than those for mMFC-6/PMS binary system. Meanwhile, the signals of TEMP-$^1O_2$ adducts in the cases of PMS or mMFC-6-containing BPB solutions could hardly be detected. These findings suggest that the formation of $^1O_2$ was mainly due to the activation/catalysis of mMFC-6 toward PMS, thus excluding the main role of direct electron abstraction coupled with subsequent oxidation in forming TEMP-$^1O_2$ adducts. The time-dependent changes of DMPO$^{\cdot}$−OH and DMPO$^{\cdot}$-$SO_4^{\cdot-}$ adduct signals (Fig. 5(a_4–a_6)) suggest the persistence of $SO_4^{\cdot-}$ and $^{\cdot}$OH in aquatic environment for BPB oxidation. However, with the reaction time increased, the TEMP-$^1O_2$ adduct signals (Fig. 5(b_4–b_6)) first increased then greatly decreased. This might be a result of the consumption of $^1O_2$ for forming $SO_4^{\cdot-}$ and $^{\cdot}$OH (discuss later).

More important, after theoretical calculations, we believed that $^1O_2$ in mMFC-6/PMS did not cause a significant BPB oxidation degradation. This is because of the following: in the light of previous work [59,60], the first-order rate constant of $^1O_2$ with 25.74 μM BPB (estimated about (2.47–9.78) × 10^2 s^{-1}) is 256–1012 times lower than with water (2.5 × 10^5 s^{-1}), which could result in only 3.83%–15.11% of BPB oxidation even when 2 mM PMS was completely catalyzed to form 1 mM $^1O_2$. Therefore, the main contribution of $^1O_2$ to BPB oxidation can be excluded, so does $O_2^{\cdot-}$ (similarly because of its lower second-order rate constant with BPB (estimated about (0.58–2.7) × 10^3 $M^{-1}s^{-1}$)) [61,62]. To further elucidate the formation of $^{\cdot}$OH, $SO_4^{\cdot-}$, $^1O_2$ and $O_2^{\cdot-}$ and the potential of $^1O_2$ and/or $O_2^{\cdot-}$ in controlling the formation/evolution of $SO_4^{\cdot-}$ and $^{\cdot}$OH, BQ, dimethylsulfoxide (DMSO, as a stabilizer for $O_2^{\cdot-}$) and furfuryl alcohol (FFA) [37,58] were used in EPR measurements. It is quite clear that, when BQ (either 5 or 20 mM) was introduced in mMFC-6/PMS system (Fig. 5(c_1–c_3, b_1–b_3)), completely disappeared signals of DMPO and TEMP adducts were observed, suggesting that $^{\cdot}$OH, $SO_4^{\cdot-}$, $^1O_2$ and $O_2^{\cdot-}$ were generated. The greatly decreased signals for DMPO$^{\cdot}$−OH, DMPO$^{\cdot}$-$SO_4^{\cdot-}$ and TEMP-$^1O_2$ adducts caused by DMSO (Fig. 5(c_4, b_4)) suggest the role of $O_2^{\cdot-}$ in controlling the formation of $^1O_2$, $SO_4^{\cdot-}$ and $^{\cdot}$OH. FFA-based EPR tests (Fig. 5(c_5, b_5)) also verify the formation of $^1O_2$ (in addition to other ROS like $^{\cdot}$OH) in mMFC-6/PMS system. Given the fact that the lifetime of $^1O_2$ can be notably prolonged in D_2O [21,63], we also compared mMFC-6 activation performance toward PMS in D_2O and H_2O to examine such role of $^1O_2$. The removal efficiency of BPB in D_2O decreased as also shown by k_{obs} value which decreased by 55.22 % (refer to Fig. S11). Considering the intrinsically low reactivity of $^1O_2$ toward BPB, we assumed that the extended lifetime of $^1O_2$ in D_2O probably delayed/suppressed the formation of $SO_4^{\cdot-}$ and/or $^{\cdot}$OH by the proposed ways of Reactions (1)–(13), thus decreasing the rate of BPB oxidation.

On the basis of the aforementioned discussion, a conceptual diagram regarding the catalytic mechanism of mMFC-6 toward PMS and the ROS evolutions was accordingly provided in Fig. 6. The exposed Mn/Fe species (metal catalytic sites) on mMFC-6 surface could catalyze PMS to generate $O_2^{\cdot-}$, $SO_4^{\cdot-}$ and/or $^{\cdot}$OH *via* an electronic transfer process (cf. Fig. 6(a_1–a_5) and Reactions (1)–(4). Meanwhile, the −C═O or defects (non-metal catalytic sites) within mMFC-6 could also catalyze PMS to form $^1O_2$ (cf. Fig. 6(b_1–b_5) and Reaction (5)). The decreasing in k_{obs} value for acid-treated mMFC-6 was used as a conservative parameter to evaluate the relative contribution of metal and non-metal catalytic sites for PMS activation (cf. Fig. S12). It was found that BPB removal clearly decreased as also shown by the k_{obs} value which decreased by 65.80 %. Therefore, it can be concluded that metal catalytic sites within mMFC-6 made more contribution to PMS activation than non-metal sites (65.8 % vs 34.2 %). It should be noted that the decreased concentration of −C═O (due to the formation of $^1O_2$ and/or the radical oxidation process (as discussed earlier)) is also beneficial for PMS activation by mMFC-6 to generate $SO_4^{\cdot-}$ and/or $^{\cdot}$OH [50]. The newly formed $O_2^{\cdot-}$ can catalyze PMS to produce $SO_4^{\cdot-}$ and/or $^{\cdot}$OH or directly induce $^1O_2$ formation (cf. Figs. 6, 5(c_2–c_4, d_2–d_4) and Reactions (6)–(13) [42,43,52,64,65]; meanwhile, the generated $^1O_2$ can regulate the formation of $SO_4^{\cdot-}$ and $^{\cdot}$OH through two processes (cf. Figs. 6 and 5(c_5,d_5)): first, the resultant $^1O_2$ increased the dissolved O_2 of reaction system by its collision with water (Reaction (13)) [66], then, the enhanced dissolved O_2 promoted the production/transformation of $SO_4^{\cdot-}$ and $^{\cdot}$OH via various circular processes (cf. Reactions (1)–(13) [42,47,52,64,65]. Lastly, the regenerated mMFC-6 continues to control the next ROS formation and $SO_4^{\cdot-}$ and $^{\cdot}$OH-mediated radical oxidation of BPB. Such catalytic processes are quite complex, and each process may act synchronously/successively to form $O_2^{\cdot-}$, $^1O_2$, $SO_4^{\cdot-}$ and/or $^{\cdot}$

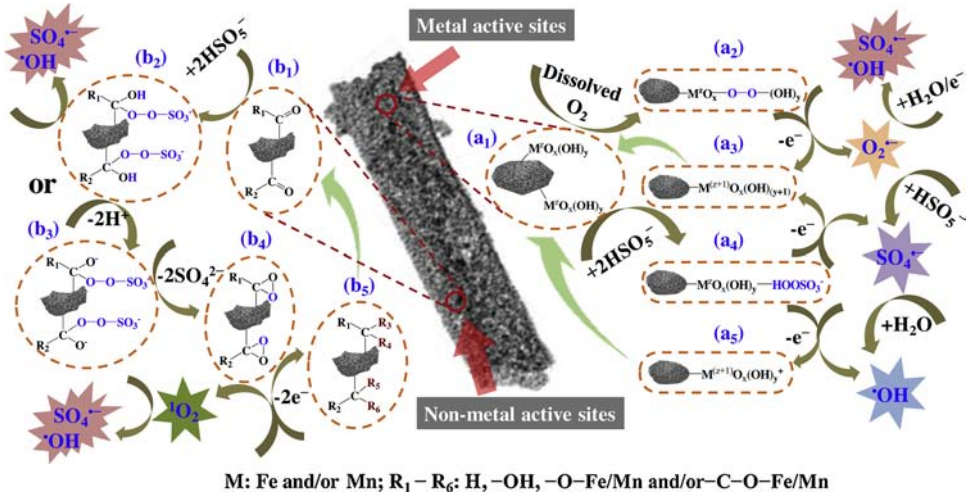

Fig. 6. Proposed mechanism for PMS activation by mMFC-6 and ROS formation.

OH (see Reactions (1)–(13)).

$$\equiv MnFeC_xO_y(OH)_z + O_2 \rightarrow \equiv MnFeC_xO_y(OH)_z^{+} + O_2^{\cdot -} \quad (1)$$

$$\equiv MnFeC_xO_y(OH)_z + HSO_5^{-} \rightarrow \equiv MnFeC_xO_y(OH)_z - HOOSO_3^{-} \quad (2)$$

$$\equiv MnFeC_xO_y(OH)_z - HOOSO_3^{-} \rightarrow \equiv MnFeC_xO_y(OH)_{z+1} + SO_4^{\cdot -} \quad (3)$$

$$\equiv MnFeC_xO_y(OH)_z - HOOSO_3^{-} \rightarrow \equiv MnFeC_xO_y(OH)_z^{+} + SO_4^{2-} + {}^{\cdot}OH \quad (4)$$

$$2\equiv MnFeC_xO_y(OH)_z - HOOSO_3^{-} \rightarrow 2\equiv MnFeC_xO_y(OH)_z + {}^1O_2 + 2HSO_4^{-} \quad (5)$$

$$\equiv MnFeC_xO_y(OH)_z + O_2^{\cdot -} + 2H^{+} \rightarrow \equiv MnFeC_xO_y(OH)_z^{+} + H_2O_2 \quad (6)$$

$${}^{\cdot}OH + {}^{\cdot}OH \rightarrow H_2O_2 \quad (7)$$

$$H_2O_2 + O_2^{\cdot -} + H^{+} \rightarrow H_2O + {}^{\cdot}OH + O_2 \quad (8)$$

$$SO_4^{\cdot -} + SO_4^{\cdot -} \rightarrow S_2O_8^{2-} \quad (9)$$

$$S_2O_8^{2-} + O_2^{\cdot -} \rightarrow SO_4^{2-} + SO_4^{\cdot -} + O_2 \quad (10)$$

$$2O_2^{\cdot -} + 2H^{+} \rightarrow H_2O_2 + {}^1O_2 \quad (11)$$

$$O_2^{\cdot -} + {}^{\cdot}OH \rightarrow {}^1O_2 + 2OH^{-} \quad (12)$$

$${}^1O_2 \rightarrow O_2 \quad (13)$$

3.3.3. Possible pathways for BPB oxidation

The intermediates for BPB oxidation by the mMFC-6/PMS system were detected using HPLC-MS/MS. The fragment spectra of BPB oxidation products (+MS model) are shown in Fig. S13. Based on the tentatively identified by-products and previously reported pathways [67], we proposed that the main pathways for BPB oxidation by the current system were as follows (Figs. S14–S16): (1) direct oxidation and/or chain cleavage/decarboxylation, resulting in the formation of products with *m/z* of 174.9 and 274.7 (cf. P_{174}-1 and P_{274}-1 in Figs. S14 and S15), (2) direct oxidation then rearrangement/dehydrogenation, leading to the formation of P_{208}-1, P_{208}-2 and P_{208}-3 (Fig. S16), (3) combined processes of oxidation, chain/ring cleavage, decarboxylation, dehydrogenation and rearrangement, causing the formation of P_{156}-1, P_{174}-1, P_{174}-2, P_{252}-1 and P_{274}-2 (Figs. S14 and S15), and (4) chain oxidation/cleavage, ring cleavage and/or dehydrogenation, making the resultant P_{208}-1, P_{208}-2 and P_{208}-3 further transferred into P_{190}-1, P_{190}-2, P_{190}-3 or P_{208}-4 (Fig. S16). After these proposed degradation processes, some of these products might be further degraded into small molecules like CO_2 via direct oxidation, ring/chain cleavage and decarboxylation.

3.4. Effect of environmental conditions

Inorganic ions, as the common environmental constituents, are ubiquitous in groundwater/wastewater, and can exert different impacts on PO-ISCO processes for contaminant oxidation [68]. Therefore, we examined the effects of commonly found Ca^{2+}, Mg^{2+}, Cl^{-}, NO_3^{-}, HCO_3^{-}, SO_4^{2-} and PO_4^{3-} at different levels on the performance of mMFC-6/PMS system. Insignificant effect of Ca^{2+} at 0–2 mM and Mg^{2+} at 0 – 0.2 mM was observed (Fig. 7(a)). However, further increasing the concentration of Mg^{2+} from 0.2 to 2 mM greatly accelerated the BPB oxidation by the mMFC-6/PMS system, which might be due to its cation bridging effect between the negatively charged hydroxy/carboxy groups within mMFC-6 and HSO_5^{-} [10]. Fig. 7(b) exhibits that, in general, Cl^{-} at 0–20 mM demonstrated varied promoting effects on the BPB oxidation. Specifically, increasing the concentration of Cl^{-} from 0 to 2 mM caused a complete BPB oxidation with the reaction time decreasing from 180 to 105 min, while further increasing it to 4 mM led to an ultra-fast and complete BPB oxidation within 5 min; however, when the concentration of Cl^{-} increased from 4 to 10 then to 20 mM, the rate of BPB oxidation first dropped down to that without Cl^{-}, then went back to that with 4 mM Cl^{-}. Previous work showed that Cl^{-} could react with ROS (especially for $SO_4^{\cdot -}$ and $^{\cdot}OH$) and HSO_5^{-} to form various chloride active species (like $Cl^{\cdot}$, $Cl_2^{\cdot -}$, Cl_2, HOCl, etc.) (cf. Reactions (14)–(23)) [68–71]. The following reaction processes probably account for the above observations. 1) At the Cl^{-} concentration of ≤ 4 mM, Cl^{-} can react with $SO_4^{\cdot -}$ and $^{\cdot}OH$ to form $Cl^{\cdot}$ and $Cl_2^{\cdot -}$ (Reactions (14)–(17)), which are highly reactive in oxidation personal care products [72], thus enhancing BPB oxidation. 2) However, at Cl^{-} concentration of 10 mM, both the large consumption of $SO_4^{\cdot -}$ and $^{\cdot}OH$ and the direct reaction of Cl^{-} with HSO_5^{-} to form less reactive Cl_2 might be the reasons for decreased degradation kinetics (Reactions (14)–(19)). 3) The presence of stable $Cl^{\cdot}$ and $Cl_2^{\cdot -}$ and the formation of HClO and $^{\cdot}OH$ at Cl^{-} concentration of 20 mM possibly attributed to the increase of degradation rates for BPB (cf. Reactions (14)–(23)). Apparently, the role of Cl^{-}-concentration in controlling BPB oxidation in mMFC-6/PMS system is a result of the trade-off between the primary ROS and the secondary chloride active species competing for BPB oxidation [3,52,64]. It is noticeable that, despite the potentially enhanced mineralization of BPB by chloride active species, some undesirable chlorinated intermediates may also form in Cl^{-}-containing solutions [50,53,73].

$$SO_4^{\cdot -} + Cl^{-} \rightarrow SO_4^{2-} + Cl^{\cdot},\ k = 3.2 \times 10^8\ M^{-1}\ s^{-1} \quad (14)$$

$$^{\cdot}OH + Cl^{-} \leftrightarrow HOCl^{\cdot -},\ k = 4.3 \times 10^9\ M^{-1}\ s^{-1} \quad (15)$$

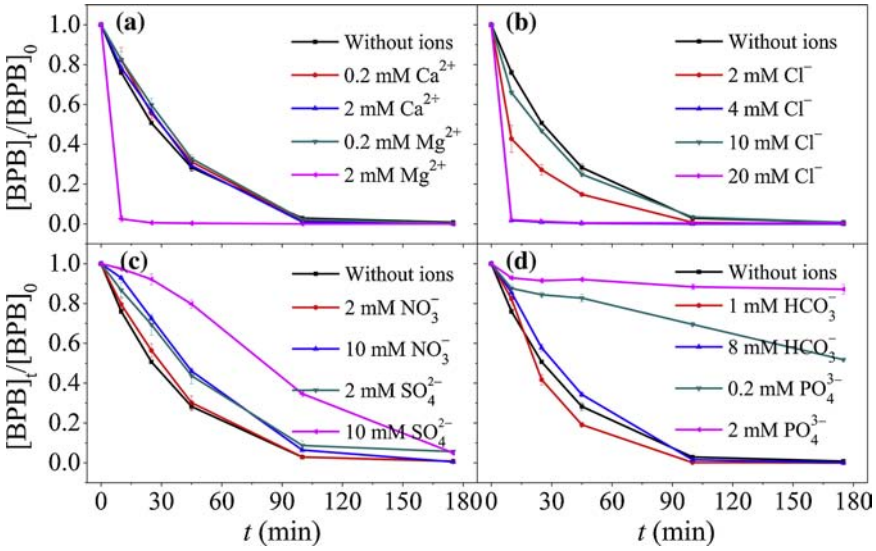

Fig. 7. Effects of the common cations (Ca^{2+} and Mg^{2+}) (a) and anions (Cl^-, NO_3^-, SO_4^{2-}, HCO_3^- and PO_4^{3-}) (b–d) on BPB oxidation by the mMFC-6/PMS system ($[mMFC\text{-}6]_0$ = 125 mg/L, $[BPB]_0$ = 25.74 μM, $[PMS]_0$ = 2 mM, $[pH]_0$ = 6.83 ± 0.20, T = 298 ± 2 K).

$$HOCl^{\cdot -} + H^+ \leftrightarrow Cl^{\cdot} + H_2O \; k = 2.6 \times 10^{10}\, M^{-1} s^{-1} \quad (16)$$

$$Cl^{\cdot} + Cl^- \leftrightarrow Cl_2^{\cdot -}, \; k = 7.8 \times 10^9\, M^{-1} s^{-1} \quad (17)$$

$$2Cl_2^{\cdot -} \rightarrow Cl_2 + 2Cl^-, \; k = 2.1 \times 10^9\, M^{-1} s^{-1} \quad (18)$$

$$2Cl^- + HSO_5^- + H^+ \rightarrow SO_4^{2-} + H_2O + Cl_2 \quad (19)$$

$$H_2O + Cl^{\cdot} \rightarrow HOCl^{\cdot -} + H^+, \; k = 2.5 \times 10^5\, s^{-1} \quad (20)$$

$$H_2O + Cl_2^{\cdot -} \rightarrow HOCl^{\cdot -} + Cl^- + H^+, \; k = 1.3 \times 10^3\, s^{-1} \quad (21)$$

$$HOCl^{\cdot -} \rightarrow {}^{\cdot}OH + Cl^-, \; k = 6.1 \times 10^9\, s^{-1} \quad (22)$$

$$H_2O + Cl_2 \rightarrow HOCl + Cl^- + H^+, \; k = 5.5\, s^{-1} \quad (23)$$

As indicated in Fig. 7(c, d), NO_3^-, SO_4^{2-} and PO_4^{3-} demonstrated an obvious suppression on BPB oxidation with the order being $NO_3^- < SO_4^{2-} < PO_4^{3-}$, while a dual-effect (i.e., either inhibiting or promoting) was observed for HCO_3^-. The inhibition of NO_3^- and SO_4^{2-} is probably because of the consumption of $SO_4^{\cdot -}$ and $^{\cdot}OH$ and the formation of secondary radicals with lower activity for BPB oxidation [47,52,64], while the inhibition caused by PO_4^{3-} is likely attributed to its robust coordination with surface catalytic sites of mMFC-6, thus greatly hindering the ROS formation of mMFC-6/PMS system [47]. The slightly enhanced effect of HCO_3^- at 1 mM might be due to its buffering effect toward the pH of mMFC-6/PMS system (see Table 1), which made mMFC-6 almost neutrally charged while HSO_5^- less negatively charged compared to the case without HCO_3^-, thus making mMFC-6 catalyze PMS to produce more ROS for BPB oxidation. On the other hand, HCO_3^- can activate PMS to form $O_2^{\cdot -}$ and $^1O_2$ [74], which probably promoted the generation of $SO_4^{\cdot -}$ and $^{\cdot}OH$ (cf. Section 3.3.2) and therefore contributed to BPB removal. When the concentration of HCO_3^- increased to 8 mM, the consumption of $SO_4^{\cdot -}$ and $^{\cdot}OH$ to generate less active $CO_3^{\cdot -}/HCO_3^{\cdot}$ occurred [52,64], which inevitably suppressed BPB oxidation.

The practical applications of mMFC-6/PMS system toward BPB oxidation were further assessed by dissolving BPB in two real water matrices. The characteristics of these water matrices are listed in Table 1. After the reaction time of 45 min, the oxidation efficiency of BPB spiked in two different waters followed the order: Real water B (81 %) > Real water A (73 %). The efficiency for BPB oxidation in Real water B is higher than that in DI water (71 %), which might result from the roles of C=O groups of dissolved organic matter or polyphenols within Real water B in promoting the catalysis of mMFC-6 toward PMS [37,50]. These findings suggest that the effects of real environmental conditions warrant an in-depth study.

3.5. Oxidation kinetics

To further understand the oxidation process, two kinetic models were employed for describing BPB oxidation by the mMFC-6/PMS system as follows.

Pseudo first-order kinetic model:

$$-\frac{d[BPB]_t}{dt} = k_{obs}[BPB]_t \quad (a)$$

Eq. (a) can be transferred into Eq. (b) by integration:

$$\ln\left(\frac{[BPB]_t}{[BPB]_0}\right) = -k_{obs}t \quad (b)$$

Langmuir-Hinshelwood (L-H) kinetic model [75].

$$-\frac{d[BPB]_t}{dt} = \frac{kK[BPB]_t}{1 + K[BPB]_t} \quad (c)$$

Eq. (c) can be simplified to Eq. (d) by integration:

$$[BPB]_t^{(1-n)} = (n-1)K_L t + [BPB]_0^{(1-n)} \quad (d)$$

where $[BPB]_0$ and $[BPB]_t$ represent the concentration of BPB (μM) at time 0 and t (min), respectively, while k_{obs} is the pseudo first-order rate constant for BPB oxidation (min^{-1}). K, k, K_L and n are the equilibrium adsorption constant (μM^{-1}), the rate constant, the apparent rate constant ($\mu M^{(1-n)} min^{-1}$), and the apparent order of the reaction for BPB oxidation, respectively, fitted by L-H kinetic model.

The feasibility of two kinetic models in the mMFC-6/PMS system for BPB oxidation under various conditions were examined. As shown in Tables S3 and S6, in some cases, the whole BPB oxidation process can well be described by the pseudo first-order kinetic model; but in the presence of interference factors, this model fails to fit the whole process, suggesting the effects of interference factors on BPB oxidation (likely by regulating ROS formation/amount, consuming highly reactive $SO_4^{\cdot -}/^{\cdot}OH$ or covering catalytic sites of mMFC). In comparison, the L-H kinetic model – which considers the interference factors-controlled reaction order and rate – can better simulate the whole process of BPB oxidation by the mMFC-6/PMS system even under relatively complex conditions (cf. Tables 2 and S6). For example, the presence of Mg^{2+} at 2 mM, Cl^- at 4 or 20 mM or PO_4^{3-} at 2 mM greatly affected BPB oxidation by the mMFC-6/PMS system (Fig. 7), making the

Table 2
Fitted results for BPB oxidation by the mMFC-6/PMS system under different conditions using the L-H kinetic model.

mMFC-6 (mg/L)	PMS (mM)	Inorganic ions	pH before reaction	pH after reaction	T (K)	Removal efficiency (%)	k_a ((mg/L)$^{(1-n)}$·min^{-1})	n	R^2
125	2	None	3.04	2.66	298	99.00	2.90E-02 ± 6.22E-04	2.17E-01	0.9852
125	2	None	4.98	2.86	298	100.00	3.59E-02 ± 7.64E-04	3.53E-01	0.9907
125	2	None	6.83	2.88	298	100.00	4.80E-02 ± 5.09E-04	3.34E-01	0.9992
125	2	None	8.93	2.92	298	100.00	3.89E-02 ± 6.79E-04	3.78E-01	0.9934
125	2	None	10.47	3.02	298	100.00	4.23E-02 ± 1.98E-04	4.68E-01	0.9996
125	2	None	6.83	2.89	283	100.00	1.10E-02 ± 7.00E-04	8.41E-01	0.9952
125	2	None	6.83	2.88	313	100.00	7.34E-02 ± 1.71E-03	2.87E-01	0.9943
62.5	2	None	6.83	2.88	298	100.00	3.93E-02 ± 2.00E-03	4.06E-01	0.9936
187.5	2	None	6.83	2.82	298	100.00	3.78E-02 ± 1.41E-03	3.30E-01	0.9917
125	1	None	6.83	3.10	298	90.99	2.09E-02 ± 2.05E-04	2.90E-01	0.9904
125	4	None	6.83	2.61	298	100.00	5.72E-02 ± 4.24E-04	2.20E-01	0.9996
125	2	0.2 mM Ca^{2+}	6.83	2.72	298	99.87	3.72E-02 ± 3.44E-03	6.53E-01	0.9964
125	2	2 mM Ca^{2+}	6.83	2.71	298	100.00	4.47E-02 ± 6.56E-03	5.24E-01	0.9973
125	2	0.2 mM Mg^{2+}	6.83	2.84	298	99.62	4.79E-02 ± 1.00E-02	4.07E-01	0.9989
125	2	2 mM Mg^{2+}	6.83	2.79	298	100.00	5.75E-01 ± 2.01E-01	1.59E+00	1.0000
125	2	2 mM Cl^-	6.83	2.87	298	100.00	3.30E-02 ± 4.52E-03	1.74E+00	0.9874
125	2	4 mM Cl^-	6.83	2.84	298	100.00	1.04E+00 ± 2.50E-01	1.96E+00	1.0000
125	2	10 mM Cl^-	6.83	2.88	298	99.22	2.79E-02 ± 1.99E-03	1.15E+00	0.9932
125	2	20 mM Cl^-	6.83	2.95	298	99.52	1.77E+00 ± 3.59E-01	2.44E+00	1.0000
125	2	2 mM NO_3^-	6.83	2.82	298	99.18	4.00E-02 ± 6.55E-03	6.06E-01	0.9989
125	2	10 mM NO_3^-	6.83	3.12	298	99.54	3.82E-02 ± 1.52E-04	3.00E-01	0.9943
125	2	1 mM HCO_3^-	6.83	6.79	298	100.00	6.05E-02 ± 8.78E-03	4.59E-01	0.9908
125	2	8 mM HCO_3^-	6.83	6.81	298	100.00	3.86E-02 ± 2.23E-04	5.55E-01	0.9974
125	2	2 mM SO_4^{2-}	6.83	2.82	298	94.38	3.21E-02 ± 2.62E-03	5.03E-01	0.9923
125	2	10 mM SO_4^{2-}	6.83	3.12	298	95.03	2.62E-02 ± 8.34E-04	7.98E-02	0.9737
125	2	0.2 mM PO_4^{3-}	6.83	3.04	298	48.21	4.00E-04 ± 2.15E-04	2.79E+00	0.9214
125	2	2 mM PO_4^{3-}	6.83	3.62	298	12.86	2.07E-26 ± 3.59E-26	3.96E+01	0.8921

oxidation process hardly fitted by the first-order kinetic model (Table S6), but the L-H kinetic model could better describe such oxidation process under extreme conditions (Table 2). It is worth pointing out that there exists a nonlinear relationship between the values of K_L and n. This is reasonable, given the fact that there exist so many uncertainties regarding how these environmental chemistry constituents affect the catalysis of mMFC-6 toward PMS and ROS formation/distribution – which needs to be probed in-depth.

4. Conclusions

We demonstrated a radical and singlet-based peroxymonosulfate (PMS) oxidation system using a novel magnetic Mn-Fe oxycarbide (mMFC) catalyst and probed its performance toward BPB oxidation for the first time. The novel mMFC exhibited excellent stability and desirable catalytic reactivity. The non-metal (−C═O groups) and metal (Mn/Fe oxides) species within mMFC as dual active sites catalyzed PMS synergistically. Quite different from the previously reported common MO/PMS systems, $SO_4^{\cdot -}$, $^{\cdot}OH$, $^1O_2$ and $O_2^{\cdot -}$ could be formed simultaneously in the newly constructed mMFC/PMS catalytic oxidation system, and the generated $^1O_2$ and/or $O_2^{\cdot -}$ could serve as a favoring driving force to promote the formation of $SO_4^{\cdot -}$ and/or $^{\cdot}OH$ for BPB oxidation. The Langmuir-Hinshelwood model can better describe BPB oxidation by the mMFC/PMS system under complex conditions. This work will enable us to construct novel and earth-abundant Mn-based composites with versatile catalytic sites, excellent stability and desirable magnetism toward PS catalysis for removing ECs from the polluted water.

Declaration of Competing Interest

The authors declare that they have no known competing financial interests or personal relationships that could have appeared to influence the work reported in this paper.

Acknowledgments

We greatly appreciate the financial supports from National Natural Science Foundation of China (Grant Nos. 51778598, 51808524 and 51478449), Fujian Provincial Key Laboratory of Ecology-Toxicological Effects & Control for Emerging Contaminants (PY18003), Science and Technology Major Project of the Bureau of Science and Technology of Xiamen (No. 3502Z20191012) and International Science & Technology Cooperation Program of China (2011DFB91710).

Appendix A. Supplementary data

Supplementary material related to this article can be found, in the online version, at doi:https://doi.org/10.1016/j.apcatb.2019.118549.

References

[1] K. Kümmerer, D.D. Dionysiou, O. Olsson, D. Fatta-Kassinos, A path to clean water, Science 361 (2018) 222–224, https://doi.org/10.1126/science.aau2405.
[2] L. Zhang, Z. Jia, F. Lyu, S. Liang, J. Lu, A review of catalytic performance of metallic glasses in wastewater treatment: recent progress and prospects, Prog. Mater. Sci. 105 (2019) 100576, https://doi.org/10.1016/j.pmatsci.2019.100576.
[3] W. Zhang, S. Zhou, J. Sun, X. Meng, J. Luo, D. Zhou, J. Crittenden, Impact of chloride ions on UV/H_2O_2 and UV/persulfate advanced oxidation processes, Environ. Sci. Technol. 52 (2018) 7380–7389, https://doi.org/10.1021/acs.est.8b01662.
[4] S. Liang, Z. Jia, Y. Liu, W. Zhang, W. Wang, J. Lu, L. Zhang, Compelling rejuvenated catalytic performance in metallic glasses, Adv. Mater. 30 (2018) 1802764, https://doi.org/10.1002/adma.201802764.
[5] S.X. Liang, Z. Jia, W.C. Zhang, X.F. Li, W.M. Wang, H.C. Lin, L.C. Zhang, Ultrafast activation efficiency of three peroxides by $Fe_{78}Si_9B_{13}$ metallic glass under photo-enhanced catalytic oxidation: a comparative study, Appl. Catal. B Environ. 221 (2018) 108–118, https://doi.org/10.1016/j.apcatb.2017.09.007.
[6] J. Kang, L. Zhou, X. Duan, H. Sun, Z. Ao, S. Wang, Degradation of cosmetic microplastics via functionalized carbon nanosprings, Matter 1 (2019) 745–758, https://doi.org/10.1016/j.matt.2019.06.004.
[7] H. Li, C. Shan, B. Pan, Fe(III)-doped g-C_3N_4 mediated peroxymonosulfate activation for selective degradation of phenolic compounds via high-valent iron-oxo species, Environ. Sci. Technol. 52 (2018) 2197–2205, https://doi.org/10.1021/acs.est.7b05563.
[8] J. Kang, H. Zhang, X. Duan, H. Sun, X. Tan, S. Liu, S. Wang, Magnetic Ni-Co alloy encapsulated N-doped carbon nanotubes for catalytic membrane degradation of emerging contaminants, Chem. Eng. J. 362 (2019) 251–261, https://doi.org/10.

1016/j.cej.2019.01.035.
[9] X. Duan, J. Kang, W. Tian, H. Zhang, S. Ho, Y. Zhu, Z. Ao, H. Sun, S. Wang, Interfacial-engineered cobalt@carbon hybrids for synergistically boosted evolution of sulfate radicals toward green oxidation, Appl. Catal. B Environ. 256 (2019) 117795, https://doi.org/10.1016/j.apcatb.2019.117795.
[10] L. Wang, J. Jiang, S. Pang, Y. Zhou, J. Li, S. Sun, Y. Gao, C. Jiang, Oxidation of bisphenol A by nonradical activation of peroxymonosulfate in the presence of amorphous manganese dioxide, Chem. Eng. J. 352 (2018) 1004–1013, https://doi.org/10.1016/j.cej.2018.07.103.
[11] S. Zhu, X. Li, J. Kang, X. Duan, S. Wang, Persulfate activation on crystallographic manganese oxides: mechanism of singlet oxygen evolution for nonradical selective degradation of aqueous contaminants, Environ. Sci. Technol. 53 (2018) 307–315, https://doi.org/10.1021/acs.est.8b04669.
[12] H. Wu, X. Xu, L. Shi, Y. Yin, L. Zhang, Z. Wu, X. Duan, S. Wang, H. Sun, Manganese oxide integrated catalytic ceramic membrane for degradation of organic pollutants using sulfate radicals, Water Res. 167 (2019) 115110, https://doi.org/10.1016/j.watres.2019.115110.
[13] Q. Liu, X. Duan, H. Sun, Y. Wang, M.O. Tade, S. Wang, Size-tailored porous spheres of manganese oxides for catalytic oxidation via peroxymonosulfate activation, J. Phys. Chem. C 120 (2016) 16871–16878, https://doi.org/10.1021/acs.jpcc.6b05934.
[14] J. Tang, J. Wang, Metal organic framework with coordinatively unsaturated sites as efficient Fenton-like catalyst for enhanced degradation of sulfamethazine, Environ. Sci. Technol. 52 (2018) 5367–5377, https://doi.org/10.1021/acs.est.8b00092.
[15] Q. Sun, M. Liu, K. Li, Y. Han, Y. Zuo, F. Chai, C. Song, G. Zhang, X. Guo, Synthesis of Fe/M (M = Mn, Co, Ni) bimetallic metal organic frameworks and their catalytic activity for phenol degradation under mild conditions, Inorg. Chem. Front. 4 (2017) 144–153, https://doi.org/10.1039/C6QI00441E.
[16] X. Li, Z. Ao, J. Liu, H. Sun, A.I. Rykov, J. Wang, Topotactic transformation of metal–organic frameworks to graphene-encapsulated transition-metal nitrides as efficient Fenton-like catalysts, ACS Nano 10 (2016) 11532–11540, https://doi.org/10.1021/acsnano.6b07522.
[17] C. Li, J. Wu, W. Peng, Z. Fang, J. Liu, Peroxymonosulfate activation for efficient sulfamethoxazole degradation by Fe_3O_4/β-FeOOH nanocomposites: coexistence of radical and non-radical reactions, Chem. Eng. J. 356 (2019) 904–914, https://doi.org/10.1016/j.cej.2018.09.064.
[18] E. Yun, H. Yoo, H. Bae, H. Kim, J. Lee, Exploring the role of persulfate in the activation process: radical precursor versus electron acceptor, Environ. Sci. Technol. 51 (2017) 10090–10099, https://doi.org/10.1021/acs.est.7b02519.
[19] X. Duan, H. Sun, S. Wang, Metal-free carbocatalysis in advanced oxidation reactions, Acc. Chem. Res. 51 (2018) 678–687, https://doi.org/10.1021/acs.accounts.7b00535.
[20] Y. Yang, G. Banerjee, G.W. Brudvig, J. Kim, J.J. Pignatello, Oxidation of organic compounds in water by unactivated peroxymonosulfate, Environ. Sci. Technol. 52 (2018) 5911–5919, https://doi.org/10.1021/acs.est.8b00735.
[21] E. Yun, J.H. Lee, J. Kim, H. Park, J. Lee, Identifying the nonradical mechanism in the peroxymonosulfate activation process: singlet oxygenation versus mediated electron transfer, Environ. Sci. Technol. 52 (2018) 7032–7042, https://doi.org/10.1021/acs.est.8b00959.
[22] H. Cui, J. Shi, B. Yuan, M. Fu, Synthesis of porous magnetic ferrite nanowires containing Mn and their application in water treatment, J. Mater. Chem. A 1 (2013) 5902–5907, https://doi.org/10.1039/c3ta01692g.
[23] Y. Zhao, H. An, J. Feng, Y. Ren, J. Ma, Impact of crystal types of $AgFeO_2$ nanoparticles on the peroxymonosulfate activation in the water, Environ. Sci. Technol. 53 (2019) 4500–4510, https://doi.org/10.1021/acs.est.9b00658.
[24] F. Ghanbari, M. Moradi, Application of peroxymonosulfate and its activation methods for degradation of environmental organic pollutants: review, Chem. Eng. J. 310 (2017) 41–62, https://doi.org/10.1016/j.cej.2016.10.064.
[25] J. Wang, S. Wang, Activation of persulfate (PS) and peroxymonosulfate (PMS) and application for the degradation of emerging contaminants, Chem. Eng. J. 334 (2018) 1502–1517, https://doi.org/10.1016/j.cej.2017.11.059.
[26] A.G. Asimakopoulos, M. Elangovan, K. Kannan, Migration of parabens, bisphenols, benzophenone-type UV filters, triclosan, and triclocarban from teethers and its implications for infant exposure, Environ. Sci. Technol. 50 (2016) 13539–13547, https://doi.org/10.1021/acs.est.6b04128.
[27] M. Ishii, M. Nakahira, T. Yamanaka, Infrared absorption spectra and cation distributions in $(Mn, Fe)_3O_4$, Solid State Commun. 11 (1972) 209–212, https://doi.org/10.1016/0038-1098(72)91162-3.
[28] X. Duan, K. O'Donnell, H. Sun, Y. Wang, S. Wang, Sulfur and nitrogen co-doped graphene for metal-free catalytic oxidation reactions, Small 11 (2015) 3036–3044, https://doi.org/10.1002/smll.201403715.
[29] Z. Chen, Z. Jiao, D. Pan, Z. Li, M. Wu, C. Shek, C.M.L. Wu, J.K.L. Lai, Recent advances in manganese oxide nanocrystals: fabrication, characterization, and microstructure, Chem. Rev. 112 (2012) 3833–3855, https://doi.org/10.1021/cr2004508.
[30] I. Ibrahim, I.O. Ali, T.M. Salama, A.A. Bahgat, M.M. Mohamed, Synthesis of magnetically recyclable spinel ferrite (MFe_2O_4, M = Zn, Co, Mn) nanocrystals engineered by sol gel-hydrothermal technology: high catalytic performances for nitroarenes reduction, Appl. Catal. B Environ. 181 (2016) 389–402, https://doi.org/10.1016/j.apcatb.2015.08.005.
[31] Z. Tan, K. Ni, G. Chen, W. Zeng, Z. Tao, M. Ikram, Q. Zhang, H. Wang, L. Sun, X. Zhu, X. Wu, H. Ji, R.S. Ruoff, Y. Zhu, Incorporating pyrrolic and pyridinic nitrogen into a porous carbon made from C_{60} molecules to obtain superior energy storage, Adv. Mater. 29 (2017) 1603414, https://doi.org/10.1002/adma.201603414.
[32] Y. Zhou, B. Xiao, S. Liu, Z. Meng, Z. Chen, C. Zou, C. Liu, F. Chen, X. Zhou, Photo-Fenton degradation of ammonia via a manganese–iron double-active component catalyst of graphene–manganese ferrite under visible light, Chem. Eng. J. 283 (2016) 266–275, https://doi.org/10.1016/j.cej.2015.07.049.
[33] C. Pereira, A.M. Pereira, C. Fernandes, M. Rocha, R. Mendes, M.P. Fernández-García, A. Guedes, P.B. Tavares, J. Grenèche, J.P. Araújo, C. Freire, Superparamagnetic MFe_2O_4 (M = Fe, Fo, Mn) nanoparticles: tuning the particle size and magnetic properties through a novel one-step coprecipitation route, Chem. Mater. 24 (2012) 1496–1504, https://doi.org/10.1021/cm300301c.
[34] X. Lu, L. Gu, J. Wang, J. Wu, P. Liao, G. Li, Bimetal-organic framework derived $CoFe_2O_4$/C porous hybrid nanorod arrays as high-performance electrocatalysts for oxygen evolution reaction, Adv. Mater. 29 (2017) 1604437, https://doi.org/10.1002/adma.201604437.
[35] A. Moses Ezhil Raj, S.G. Victoria, V.B. Jothy, C. Ravidhas, J. Wollschl Ger, M. Suendorf, M. Neumann, M. Jayachandran, C. Sanjeeviraja, XRD and XPS characterization of mixed valence Mn_3O_4 hausmannite thin films prepared by chemical spray pyrolysis technique, Appl. Surf. Sci. 256 (2010) 2920–2926, https://doi.org/10.1016/j.apsusc.2009.11.051.
[36] M.C. Biesinger, B.P. Payne, A.P. Grosvenor, L.W.M. Lau, A.R. Gerson, R.S.C. Smart, Resolving surface chemical states in XPS analysis of first row transition metals, oxides and hydroxides: Cr, Mn, Fe, Co and Ni, Appl. Surf. Sci. 257 (2011) 2717–2730, https://doi.org/10.1016/j.apsusc.2010.10.051.
[37] Y. Zhou, J. Jiang, Y. Gao, J. Ma, S. Pang, J. Li, X. Lu, L. Yuan, Activation of peroxymonosulfate by benzoquinone: a novel nonradical oxidation process, Environ. Sci. Technol. 49 (2015) 12941–12950, https://doi.org/10.1021/acs.est.5b03595.
[38] M. Li, Y. Liu, S. Liu, D. Shu, G. Zeng, X. Hu, X. Tan, L. Jiang, Z. Yan, X. Cai, Cu(II)-influenced adsorption of ciprofloxacin from aqueous solutions by magnetic graphene oxide/nitrilotriacetic acid nanocomposite: competition and enhancement mechanisms, Chem. Eng. J. 319 (2017) 219–228, https://doi.org/10.1016/j.cej.2017.03.016.
[39] J.E. Yang, H. Lan, X. Lin, B. Yuan, M. Fu, Synthetic conditions-regulated catalytic Oxone efficacy of MnO_x/SBA-15 towards butyl paraben (BPB) removal under heterogeneous conditions, Chem. Eng. J. 289 (2016) 296–305, https://doi.org/10.1016/j.cej.2016.01.007.
[40] Y. Guan, J. Ma, X. Li, J. Fang, L. Chen, Influence of pH on the formation of sulfate and hydroxyl radicals in the UV/peroxymonosulfate system, Environ. Sci. Technol. 45 (2011) 9308–9314, https://doi.org/10.1021/es2017363.
[41] R. Daghrir, A. Dimboukou-Mpira, B. Seyhi, P. Drogui, Photosonochemical degradation of butyl-paraben: optimization, toxicity and kinetic studies, Sci. Total Environ. 490 (2014) 223–234, https://doi.org/10.1016/j.scitotenv.2014.05.006.
[42] G. Fang, D.D. Dionysiou, S.R. Al-Abed, D. Zhou, Superoxide radical driving the activation of persulfate by magnetite nanoparticles: implications for the degradation of PCBs, Appl. Catal. B Environ. 129 (2013) 325–332, https://doi.org/10.1016/j.apcatb.2012.09.042.
[43] X. Cheng, H. Guo, Y. Zhang, X. Wu, Y. Liu, Non-photochemical production of singlet oxygen via activation of persulfate by carbon nanotubes, Water Res. 113 (2017) 80–88, https://doi.org/10.1016/j.watres.2017.02.016.
[44] Ministry of Environmental Protection of the People's Republic China, Discharge Standard of Pollutants for Municipal Wastewater Treatment Plant, GB 18918-2002, (2002).
[45] T. Zhang, H. Zhu, J. Croué, Production of sulfate radical from peroxymonosulfate induced by a magnetically separable $CuFe_2O_4$ spinel in water: efficiency, stability, and mechanism, Environ. Sci. Technol. 47 (2013) 2784–2791, https://doi.org/10.1021/es304721g.
[46] J. Gonzalez, M. Torrent-Sucarrat, J.M. Anglada, The reactions of SO_3 with HO_2 radical and $H_2O\cdots HO_2$ radical complex. Theoretical study on the atmospheric formation of HSO_5 and H_2SO_4, Phys. Chem. Chem. Phys. 12 (2010) 2116–2125, https://doi.org/10.1039/b916659a.
[47] J.E. Yang, B. Yuan, H. Cui, S. Wang, M. Fu, Modulating Oxone-MnO_x/silica catalytic systems towards ibuprofen degradation: insights into system effects, reaction kinetics and mechanisms, Appl. Catal. B Environ. 205 (2017) 327–339, https://doi.org/10.1016/j.apcatb.2016.12.046.
[48] T. Zhang, Y. Chen, Y. Wang, J. Le Roux, Y. Yang, J. Croué, Efficient peroxydisulfate activation process not relying on sulfate radical generation for water pollutant degradation, Environ. Sci. Technol. 48 (2014) 5868–5875, https://doi.org/10.1021/es501218f.
[49] Y. Ren, L. Lin, J. Ma, J. Yang, J. Feng, Z. Fan, Sulfate radicals induced from peroxymonosulfate by magnetic ferrospinel MFe_2O_4 (M = Co, Cu, Mn, and Zn) as heterogeneous catalysts in the water, Appl. Catal. B Environ. 165 (2015) 572–578, https://doi.org/10.1016/j.apcatb.2014.10.051.
[50] Y. Wang, Z. Ao, H. Sun, X. Duan, S. Wang, Activation of peroxymonosulfate by carbonaceous oxygen groups: experimental and density functional theory calculations, Appl. Catal. B Environ. 198 (2016) 295–302, https://doi.org/10.1016/j.apcatb.2016.05.075.
[51] Z. Wang, L. Sun, X. Lou, F. Yang, M. Feng, Chemical instability of graphene oxide following exposure to highly reactive radicals in advanced oxidation processes, J. Colloid Interface Sci. 507 (2017) 51–58, https://doi.org/10.1016/j.jcis.2017.07.105.
[52] G.V. Buxton, C.L. Greenstock, W.P. Helman, A.B. Ross, Critical review of rate constants for reactions of hydrated electrons, hydrogen atoms and hydroxyl radicals (·OH/·O−) in aqueous solution, J. Phys. Chem. Ref. Data 17 (1988) 513–886, https://doi.org/10.1063/1.555805.
[53] R. Luo, M. Li, C. Wang, M. Zhang, M.A. Nasir Khan, X. Sun, J. Shen, W. Han, L. Wang, J. Li, Singlet oxygen-dominated non-radical oxidation process for efficient degradation of bisphenol A under high salinity condition, Water Res. 148 (2019) 416–424, https://doi.org/10.1016/j.watres.2018.10.087.
[54] R.A. Floyd, L.M. Soong, Spin trapping in biological systems. Oxidation of the spin trap 5,5-dimethyl-1-pyrroline-1-oxide by a hydroperoxide-hematin-system,

Biochem. Biophys. Res. Commun. 74 (1977) 79–84, https://doi.org/10.1016/0006-291X(77)91377-8.
[55] G. Fang, C. Liu, Y. Wang, D.D. Dionysiou, D. Zhou, Photogeneration of reactive oxygen species from biochar suspension for diethyl phthalate degradation, Appl. Catal. B Environ. 214 (2017) 34–45, https://doi.org/10.1016/j.apcatb.2017.05.036.
[56] Y. Kirino, T. Ohkuma, T. Kwan, Spin trapping with 5,5-dimethylpyrroline-n-oxide in aqueous solution, Chem. Pharm. Bull. 29 (1981) 29–34, https://doi.org/10.1248/cpb.29.29.
[57] Y. Wang, H. Sun, H.M. Ang, M.O. Tadé, S. Wang, 3D-hierarchically structured $MnO_2$for catalytic oxidation of phenol solutions by activation of peroxymonosulfate: Structure dependence and mechanism, Appl. Catal. B Environ. 164 (2015) 159–167, https://doi.org/10.1016/j.apcatb.2014.09.004.
[58] P. Liang, C. Zhang, X. Duan, H. Sun, S. Liu, M.O. Tade, S. Wang, An insight into metal organic framework derived N-doped graphene for the oxidative degradation of persistent contaminants: formation mechanism and generation of singlet oxygen from peroxymonosulfate, Environ. Sci. Nano 4 (2017) 315–324, https://doi.org/10.1039/C6EN00633G.
[59] S. Mostafa, F.L. Rosario-Ortiz, Singlet oxygen formation from wastewater organic matter, Environ. Sci. Technol. 47 (2013) 8179–8186, https://doi.org/10.1021/es401814s.
[60] P.G. Tratnyek, J. Hoigne, Oxidation of substituted phenols in the environment: a QSAR analysis of rate constants for reaction with singlet oxygen, Environ. Sci. Technol. 25 (1991) 1596–1604, https://doi.org/10.1021/es00021a011.
[61] Z. Kozmér, E. Arany, T. Alapi, E. Takács, L. Wojnárovits, A. Dombi, Determination of the rate constant of hydroperoxyl radical reaction with phenol, Radiat. Phys. Chem. 102 (2014) 135–138, https://doi.org/10.1016/j.radphyschem.2014.04.029.
[62] Y. Tsujimoto, H. Hashizume, M. Yamazaki, Superoxide radical scavenging activity of phenolic compounds, Int. J. Biochem. 25 (1993) 491, https://doi.org/10.1016/0020-711X(93)90655-X.
[63] F. Wilkinson, W.P. Helman, A.B. Ross, Rate constants for the decay and reactions of the lowest electronically excited singlet state of molecular oxygen in solution. An expanded and revised compilation, J. Phys. Chem. Ref. Data 24 (1995) 663–677, https://doi.org/10.1063/1.555965.
[64] P. Neta, R.E. Huie, A.B. Ross, Rate constants for reactions of inorganic radicals in aqueous solution, J. Phys. Chem. Ref. Data 17 (1988) 1027–1284, https://doi.org/10.1063/1.555808.
[65] B.H.J. Bielski, D.E. Cabelli, R.L. Arudi, A.B. Ross, Reactivity of HO_2/O_2^- radicals in aqueous solution, J. Phys. Chem. Ref. Data 14 (1985) 1041–1100, https://doi.org/10.1063/1.555739.
[66] F.E. Scully, J. Hoigné, Rate constants for reactions of singlet oxygen with phenols and other compounds in water, Chemosphere 16 (1987) 681–694, https://doi.org/10.1016/0045-6535(87)90004-X.
[67] J. Zhang, B. Sun, X. Xiong, N. Gao, W. Song, E. Du, X. Guan, G. Zhou, Removal of emerging pollutants by Ru/TiO_2-catalyzed permanganate oxidation, Water Res. 63 (2014) 262–270, https://doi.org/10.1016/j.watres.2014.06.028.
[68] H.V. Lutze, N. Kerlin, T.C. Schmidt, Sulfate radical-based water treatment in presence of chloride: formation of chlorate, inter-conversion of sulfate radicals into hydroxyl radicals and influence of bicarbonate, Water Res. 72 (2015) 349–360, https://doi.org/10.1016/j.watres.2014.10.006.
[69] G. Fang, D.D. Dionysiou, Y. Wang, S.R. Al-Abed, D. Zhou, Sulfate radical-based degradation of polychlorinated biphenyls: effects of chloride ion and reaction kinetics, J. Hazard. Mater. 227–228 (2012) 394–401, https://doi.org/10.1016/j.jhazmat.2012.05.074.
[70] R. Yuan, S.N. Ramjaun, Z. Wang, J. Liu, Effects of chloride ion on degradation of Acid Orange 7 by sulfate radical-based advanced oxidation process: implications for formation of chlorinated aromatic compounds, J. Hazard. Mater. 196 (2011) 173–179, https://doi.org/10.1016/j.jhazmat.2011.09.007.
[71] Y. Yang, J.J. Pignatello, J. Ma, W.A. Mitch, Comparison of halide impacts on the efficiency of contaminant degradation by sulfate and hydroxyl radical-based advanced oxidation processes (AOPs), Environ. Sci. Technol. 48 (2014) 2344–2351, https://doi.org/10.1021/es404118q.
[72] Y. Lei, S. Cheng, N. Luo, X. Yang, T. An, Rate constants and mechanisms of the reactions of Cl· and Cl_2·− with trace organic contaminants, Environ. Sci. Technol. 53 (2019) 11170–11182, https://doi.org/10.1021/acs.est.9b02462.
[73] Y. Yang, J.J. Pignatello, J. Ma, W.A. Mitch, Effect of matrix components on UV/H_2O_2 and UV/$S_2O_8^{2-}$ advanced oxidation processes for trace organic degradation in reverse osmosis brines from municipal wastewater reuse facilities, Water Res. 89 (2016) 192–200, https://doi.org/10.1016/j.watres.2015.11.049.
[74] M. Nie, W. Zhang, C. Yan, W. Xu, L. Wu, Y. Ye, Y. Hu, W. Dong, Enhanced removal of organic contaminants in water by the combination of peroxymonosulfate and carbonate, Sci. Total Environ. 647 (2019) 734–743, https://doi.org/10.1016/j.scitotenv.2018.08.065.
[75] N.G. Asenjo, R. Santamaría, C. Blanco, M. Granda, P. Álvarez, R. Menéndez, Correct use of the Langmuir–Hinshelwood equation for proving the absence of a synergy effect in the photocatalytic degradation of phenol on a suspended mixture of titania and activated carbon, Carbon 55 (2013) 62–69, https://doi.org/10.1016/j.carbon.2012.12.010.